NASA/TM—2006-214357

Development and Testing of an Axial Halbach Magnetic Bearing

Dennis J. Eichenberg, Christopher A. Gallo, and William K. Thompson
Glenn Research Center, Cleveland, Ohio

July 2006

NASA STI Program . . . in Profile

Since its founding, NASA has been dedicated to the advancement of aeronautics and space science. The NASA Scientific and Technical Information (STI) program plays a key part in helping NASA maintain this important role.

The NASA STI Program operates under the auspices of the Agency Chief Information Officer. It collects, organizes, provides for archiving, and disseminates NASA's STI. The NASA STI program provides access to the NASA Aeronautics and Space Database and its public interface, the NASA Technical Reports Server, thus providing one of the largest collections of aeronautical and space science STI in the world. Results are published in both non-NASA channels and by NASA in the NASA STI Report Series, which includes the following report types:

- TECHNICAL PUBLICATION. Reports of completed research or a major significant phase of research that present the results of NASA programs and include extensive data or theoretical analysis. Includes compilations of significant scientific and technical data and information deemed to be of continuing reference value. NASA counterpart of peer-reviewed formal professional papers but has less stringent limitations on manuscript length and extent of graphic presentations.

- TECHNICAL MEMORANDUM. Scientific and technical findings that are preliminary or of specialized interest, e.g., quick release reports, working papers, and bibliographies that contain minimal annotation. Does not contain extensive analysis.

- CONTRACTOR REPORT. Scientific and technical findings by NASA-sponsored contractors and grantees.

- CONFERENCE PUBLICATION. Collected papers from scientific and technical conferences, symposia, seminars, or other meetings sponsored or cosponsored by NASA.

- SPECIAL PUBLICATION. Scientific, technical, or historical information from NASA programs, projects, and missions, often concerned with subjects having substantial public interest.

- TECHNICAL TRANSLATION. English-language translations of foreign scientific and technical material pertinent to NASA's mission.

Specialized services also include creating custom thesauri, building customized databases, organizing and publishing research results.

For more information about the NASA STI program, see the following:

- Access the NASA STI program home page at *http://www.sti.nasa.gov*

- E-mail your question via the Internet to *help@sti.nasa.gov*

- Fax your question to the NASA STI Help Desk at 301–621–0134

- Telephone the NASA STI Help Desk at 301–621–0390

- Write to:
  NASA STI Help Desk
  NASA Center for AeroSpace Information
  7121 Standard Drive
  Hanover, MD 21076–1320

NASA/TM—2006-214357

Development and Testing of an Axial Halbach Magnetic Bearing

Dennis J. Eichenberg, Christopher A. Gallo, and William K. Thompson
Glenn Research Center, Cleveland, Ohio

National Aeronautics and
Space Administration

Glenn Research Center
Cleveland, Ohio 44135

July 2006

Acknowledgments

The project manager for this work was James F. Walker. The authors would like to thank Dawn C. Emerson, NASA Glenn Research Center, for assistance with the development of the analytical models; and Mark Christini, Ansoft Inc., for assistance with the finite element analyses.

This work was sponsored by the Fundamental Aeronautics Program at the NASA Glenn Research Center.

Level of Review: This material has been technically reviewed by technical management.

Available from

NASA Center for Aerospace Information
7121 Standard Drive
Hanover, MD 21076–1320

National Technical Information Service
5285 Port Royal Road
Springfield, VA 22161

Available electronically at http://gltrs.grc.nasa.gov

Development and Testing of an Axial Halbach Magnetic Bearing

Dennis J. Eichenberg, Christopher A. Gallo, and William K. Thompson
National Aeronautics and Space Administration
Glenn Research Center
Cleveland, Ohio 44135

Abstract

The NASA John H. Glenn Research Center has developed and tested a revolutionary Axial Halbach Magnetic Bearing. The objective of this work is to develop a viable non-contact magnetic thrust bearing utilizing Halbach arrays for all-electric flight, and many other applications. This concept will help to reduce harmful emissions, reduce the Nation's dependence on fossil fuels and mitigate many of the concerns and limitations encountered in conventional axial bearings such as bearing wear, leaks, seals and friction loss. The Axial Halbach Magnetic Bearing is inherently stable and requires no active feedback control system or superconductivity as required in many magnetic bearing designs. The Axial Halbach Magnetic Bearing is useful for very high speed applications where conventional bearings cannot be used including turbines, instrumentation, and medical applications. In addition, this technology has potential application in ultra-efficient motors, computer memory systems, manufacturing equipment and space power systems such as flywheels.

Introduction

The NASA Glenn Research Center has a wealth of experience in Halbach bearing technology through the Fundamental Aeronautics Program. The goals of the program include improving aircraft efficiency, reliability, and safety. The Axial Halbach Magnetic Bearing was developed under the Fundamental Aeronautics Program.

The electromagnetic concept uses permanent magnet elements attached to the side of the rotor, and wire coils placed in the stator shell. The permanent magnets are arranged in a "Halbach" configuration which results in the production of a sinusoidally varying, periodic magnetic field in the vicinity of the stator coils. This magnetic array configuration was pioneered by Klaus Halbach for use in particle accelerators. When set in motion, the time varying magnetic fields interact with the passive coils in the stator assembly to produce repulsive forces between the stator and the rotor providing magnetic suspension. The advantage of this technique is that it is inherently stable once the rotor reaches a critical speed, and thus requires no active feedback control or superconductivity as seen in many traditional implementations of magnetic suspension.

Theoretical derivations have been developed to predict the levitation forces generated by a circular Halbach array and coil assembly. Finite element analyses were performed to validate the theoretical derivations. Experimental hardware was successfully designed and developed which served to validate the basic principles described and the theoretical work that was performed.

In addition to aircraft engines, this technology has potential application in ultra-efficient motors, computer memory systems, instrumentation systems, medical systems, manufacturing equipment, and space power systems, such as generators and flywheels.

Electromagnetic Analysis of The Axial Halbach Magnetic Bearing

Magnetostatic Field

Figure 1 shows a typical arrangement of magnets comprising an axial Halbach array. In this case there are $N_m = 32$ sector-shaped permanent magnets with inner radius r_1, outer radius r_2 and axial thickness T. There are four magnets per Halbach wavelength in the azimuthal (i.e.,ϕ) direction. Each magnet has an index, $s = [0, 1, \ldots N_m\text{-}1]$. The magnets each have a magnetization $M = \pm 4\pi B_r/\mu_o$ whose direction is indicated by the arrows. B_r is the remanent magnetization of the permanent magnet material.

Consider two overlapping coordinate systems, one Cartesian and the other cylindrical. The cylindrical r-ϕ plane aligns with the Cartesian x-y plane, so that the z coordinates of each system are identical. The $+x$ axis of the Cartesian system lies at $\phi = 0$ in the cylindrical system. In both coordinate systems the $+z$ axis corresponds to the axis of rotation and the flat bottom faces of the sectors lie at axial position $z_1 = 0$ with $z_2 = T$. The $s = 0$ magnet is magnetized in the axial ($+z$) direction. The $+x$ axis bisects the flat bottom surface of this magnet. Magnets lying on the $-x$, $+y$, and $-y$ axes are also magnetized in this direction. The sth magnet has a central radial axis lying at angle $\beta_s = 2\pi s/N_m$. Each magnet subtends an angle in the ϕ direction of $\beta_2 - \beta_1 = 2\pi/N_m$ radians, where β_2 and β_1 are the locations of the side faces.

The magnetic field component solutions at an arbitrary point in space are expressed in cylindrical coordinates as

$$\vec{B}(r,\phi,z) = \{B_r, B_\phi, B_z\} \tag{1}$$

with an equivalent Cartesian representation of

$$\vec{B}(x,y,z) = \{B_r \cos\phi - B_\phi \sin\phi, \quad B_r \sin\phi + B_\phi \cos\phi, \quad B_z\} \tag{2}$$

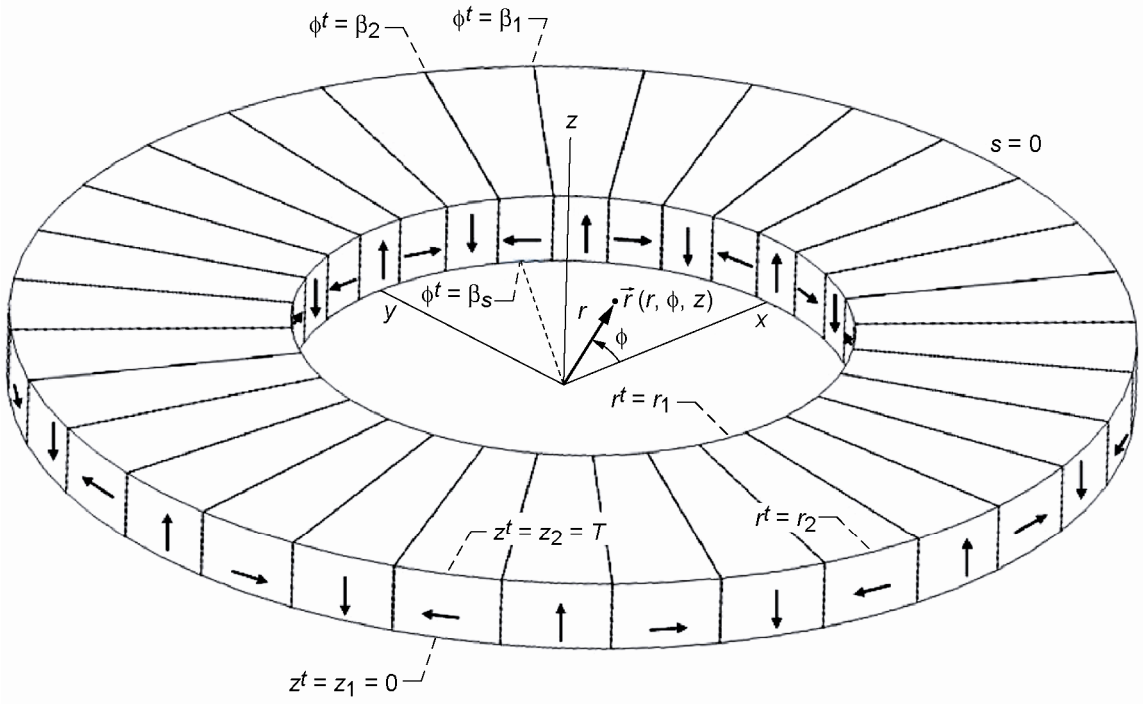

Figure 1.—The axial Halbach array for $N_m = 32$ magnets. Arrows indicate the direction of magnetization for each individual magnet. This particular arrangement will concentrate the B field below the ring and cancel it above the ring.

Using the principle of linear superposition, the aggregate field components become the sum of individual contributions from equivalent surface currents on the faces of each sector in the array. This method of analysis derives the *B* field as the curl of the vector potential, as performed in (ref. 1). The expressions for the field components in the cylindrical system at a spatial location $\vec{r} = (r\hat{r} + \phi\hat{\phi} + z\hat{z})$ become:

$$B_r(\vec{r}) = \frac{\mu_o M}{4\pi} \sum_{n=0}^{\frac{N_m}{2}-1} (-1)^n \sum_{j=1}^{2} (-1)^j \left[\begin{array}{l} \left[\int_{z_1}^{z_2} \int_{\beta_1=\frac{(4n-1)\pi}{N_m}}^{\beta_2=\frac{(4n+1)\pi}{N_m}} \frac{(z-z')\cos(\phi-\phi')}{|\vec{r}-\vec{r}'|^3} r' \, d\phi' \, dz' \right]_{r'=r_j} + \\ \left[\int_{z_1}^{z_2} \int_{r_1}^{r_2} \frac{(z-z')\sin(\phi-\phi')}{|\vec{r}-\vec{r}'|^3} dr' \, dz' \right]_{\phi'=\beta_j=\frac{(4n+2j-3)\pi}{N_m}} + \\ \left[\int_{z_1}^{z_2} \int_{\beta_1=\frac{(4n+1)\pi}{N_m}}^{\beta_2=\frac{(4n+3)\pi}{N_m}} \frac{\sin(\phi-\phi')}{|\vec{r}-\vec{r}'|^3} r'^2 \, d\phi' \, dz' \right]_{r'=r_j} - \\ \left[\int_{r_1}^{r_2} \int_{\beta_1=\frac{(4n+1)\pi}{N_m}}^{\beta_2=\frac{(4n+3)\pi}{N_m}} \frac{(z-z')\sin(\phi-\phi')}{|\vec{r}-\vec{r}'|^3} r' \, d\phi' \, dr' \right]_{z'=z_j} \end{array} \right] \tag{3}$$

$$B_\phi(\vec{r}) = \frac{\mu_o M}{4\pi} \sum_{n=0}^{\frac{N_m}{2}-1} (-1)^n \sum_{j=1}^{2} (-1)^{j+1} \left[\begin{array}{l} \left[\int_{z_1}^{z_2} \int_{\beta_1=\frac{(4n-1)\pi}{N_m}}^{\beta_2=\frac{(4n+1)\pi}{N_m}} \frac{(z-z')\sin(\phi-\phi')}{|\vec{r}-\vec{r}'|^3} r' \, d\phi' \, dz' \right]_{r'=r_j} - \\ \left[\int_{z_1}^{z_2} \int_{r_1}^{r_2} \frac{(z-z')\cos(\phi-\phi')}{|\vec{r}-\vec{r}'|^3} dr' \, dz' \right]_{\phi'=\beta_j=\frac{(4n+2j-3)\pi}{N_m}} + \\ \left[\int_{r_1}^{r_2} \int_{\beta_1=\frac{(4n+1)\pi}{N_m}}^{\beta_2=\frac{(4n+3)\pi}{N_m}} \frac{(z-z')\cos(\phi-\phi')}{|\vec{r}-\vec{r}'|^3} r' \, d\phi' \, dr' \right]_{z'=z_j} + \\ \left[\int_{z_1}^{z_2} \int_{\beta_1=\frac{(4n+1)\pi}{N_m}}^{\beta_2=\frac{(4n+3)\pi}{N_m}} \frac{(r-r'\cos(\phi-\phi'))}{|\vec{r}-\vec{r}'|^3} r' \, d\phi' \, dz' \right]_{r'=r_j} \end{array} \right] \tag{4}$$

$$B_z(\vec{r}) = \frac{\mu_o M}{4\pi} \sum_{n=0}^{\frac{N_m}{2}-1} (-1)^n \sum_{j=1}^{2} (-1)^{j+1} \left[\begin{array}{l} \left[\int_{z_1}^{z_2} \int_{\beta_1=\frac{(4n-1)\pi}{N_m}}^{\beta_2=\frac{(4n+1)\pi}{N_m}} \frac{r\cos(\phi-\phi') - r'}{|\vec{r}-\vec{r}'|^3} r' d\phi' dr' \right]_{r'=r_j} + \\ \left[\int_{z_1}^{z_2} \int_{r_1}^{r_2} \frac{r\sin(\phi-\phi')}{|\vec{r}-\vec{r}'|^3} dr' dz' \right]_{\phi'=\beta_j=\frac{(4n+2j-3)\pi}{N_m}} - \\ \left[\int_{r_1}^{r_2} \int_{\beta_1=\frac{(4n+1)\pi}{N_m}}^{\beta_2=\frac{(4n+3)\pi}{N_m}} \frac{r\sin(\phi-\phi')}{|\vec{r}-\vec{r}'|^3} r' d\phi' dr' \right]_{z'=z_j} \end{array} \right] \quad (5)$$

These functions do not necessarily have closed form solutions, but their numerical implementation is relatively straightforward in a variety of commercial mathematical analysis software packages. *Mathematica* v5.2 provided the results for this paper.

As demonstrated elsewhere (ref. 1), at sufficiently large values of gap distance g, each of the three field components exhibits sinusoidal behavior versus azimuthal position, ϕ Additional harmonics in the field components arise at axial distances that are small compared to the magnet thickness. However, for a large enough stator winding these harmonics are smoothed out in the flux calculations. All three field components also exhibit decaying exponential behavior with increasing gap distance, g.

It would be desirable to arrive at a closed form approximation for the dynamic behavior of the rotating array. However, as we shall see, the dependence of the field components as well as the Halbach wave number and the stator winding factor on radial position complicates this approach. It is therefore necessary to compute the flux numerically through a winding of known spatial position and properties.

Note that both the $B_\phi(r)$ and $B_z(r)$ field components are available for linking flux in the stator winding. An *r-z* flux plane links the B_ϕ field, and an *r-*ϕ flux plane links the B_z field. The following analyses consider both choices for the orientation of the stator winding.

Flux, EMF, Current and Force Calculations for an *r-z* Stator Pole Piece

First, position the axial Halbach array just above a stator pole piece which is sector shaped and wound vertically, i.e., the plane of the center of the stator winding lies in the *r-z* plane at azimuthal location $\phi = 0$. The normal vector of this plane coincides with the ϕ direction. The winding consists of N_t turns that are wound as radial spokes pointing toward the central axis of rotation of the array. The width of the winding in the radial direction is W and the height in the axial direction is H. W is chosen to be approximately the magnet width. H is chosen so as to optimally trade off between making the Lorentz force interaction between the returning current and the B_ϕ field as small as practical while minimizing the stator resistance, which tends to reduce the lifting force and increase the drag force and power dissipation. A gap, g, exists between the bottom surface of the magnets and the center of the top conductors of the winding. The axial location of the top of the winding is $Z_2 = -g$ and the bottom is located at $Z_1 = -(g + H)$. Figure 2 illustrates these concepts from a view located below the winding.

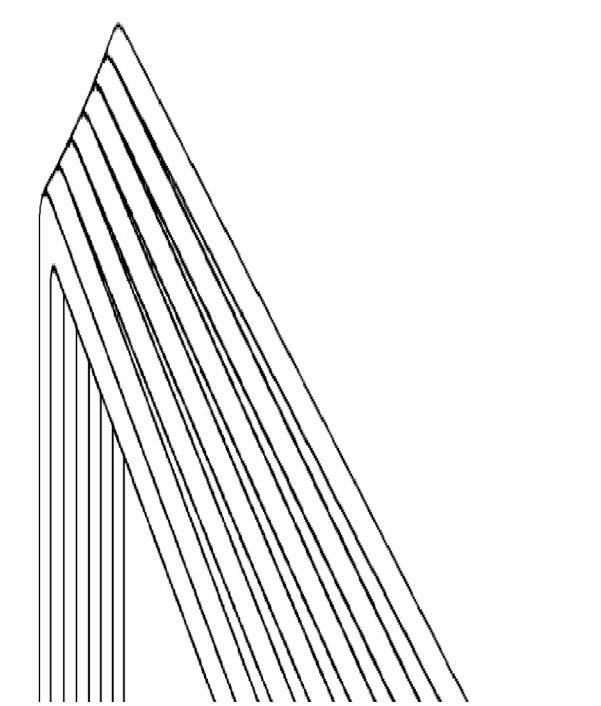

Figure 2.—The r-z stator winding viewed from below the magnet array. The azimuthal span of the winding matches the width of one magnet. H and W refer to the winding height and width, respectively. A gap, g, (not shown) exists between the conductors of the winding and the magnet surface.

The stator flux is calculated numerically by integrating the field component normal to the winding plane over the surface enclosed by the stator winding. For an *r-z* winding the flux as a function of angular position is given by

$$\Phi_{r-z}(\phi) = N_t w \int_S B_\phi(\vec{r}) \bullet dS = N_t w \int_{Z_1}^{Z_2} \int_{R_1}^{R_2} B_\phi(r, \phi, z)\, dr\, dz \tag{6}$$

using $Z_2 = -g$ and $Z_1 = -(g + H)$ and $W = R_2 - R_1 = r_2 - r_1$. The winding factor, $w = w_1 w_2$, accounts for the spatial variance of the B field over the azimuthal span and the axial depth of the winding, respectively. Two properties of the B field determine the two winding factor components. First, only the fundamental sinusoidal component of the field versus azimuthal position will contribute to force production. The first winding factor component w_1 then becomes the average over all winding turns when the peak of a cosine function coincides with the center of the winding. Secondly, the B field decays exponentially with axial position according to the Halbach wave number, k (refs. 1 and 2). The second winding factor, w_2, then becomes the average over all layers of this axial decay factor when the top layer is normalized to unity. For a stator winding of N_{tz} layers with $N_{t\phi}$ turns in each layer, there are $N_t = N_{tz} N_{t\phi}$ total turns. The first winding factor component w_1 is therefore given by:

$$w_1 = \begin{cases} \dfrac{2}{N_{t\phi}} \displaystyle\sum_{n=0}^{\frac{N_{t\phi}}{2}-1} \cos\left(\dfrac{(n+\frac{1}{2})(d+\varepsilon)}{4R_1 / N_m} \right) & for\ N_{t\phi}\ even \\ \dfrac{1}{N_{t\phi}} \left[1 + 2 \displaystyle\sum_{n=1}^{\frac{N_{t\phi}-1}{2}} \cos\left(\dfrac{n(d+\varepsilon)}{4R_1 / N_m} \right) \right] & for\ N_{t\phi}\ odd \end{cases} \tag{7}$$

and the second component w_2 is given by

$$w_2(r) = \frac{1}{N_{tz}} \sum_{n=0}^{N_{tz}-1} e^{-k(r)n(d+\varepsilon)} \tag{8}$$

where d is the diameter of the conductor comprising the stator winding, ε is the average distance between the individual turns, and R_1 is the inner radial position of the winding. Unlike a linear Halbach array (ref. 2) or even a radial Halbach array, the axial Halbach array presents a unique situation because k is not a constant but a function of radial position given by,

$$k(r) = N_m / 4r \tag{9}$$

If the winding spans approximately the same angle as one magnet and $N = 1$ layer, then $w \approx 0.9$ and this factor may be taken outside the integral. For other winding geometries the winding factor may be computed as a spatial average over the radial span and axial depth of the winding and then taken outside the integral.

Using the sinusoidal nature of the flux versus azimuthal position to solve equation (1) numerically for the maximum flux (at an angular position $\phi = 2\pi/N_m$) gives an approximation to the flux as

$$\hat{\Phi}_{r-z}(\phi) = \left[\Phi_{r-z}(\phi)\big|_{\phi=0} \right] \cos\left(\frac{N_m}{4}\phi \right) = \Phi_{\max,r-\phi} \cos\left(\frac{N_m}{4}\phi \right) \tag{10}$$

Assume that the array now rotates at a constant angular velocity $\omega = 2\pi \times$ rpm/60, where rpm is the rotational speed expressed in revolutions per minute. The initial rotary position of the array relative to the static Halbach array case is ϕi. Therefore the spatial component ϕ of the vector $\vec{r}\ (r,\phi,z)$ is now a function of time such that

$$\phi = \phi_i - \omega t \tag{11}$$

and the field components therefore become sinusoidal functions of time

$$B_\phi(r,-\omega t,z) = -B_{\phi o}(r) e^{-k(r)z} \sin(\omega t) \tag{12}$$

$$B_z(r,-\omega t,z) = B_{zo}(r) e^{-k(r)z} \cos(\omega t) \tag{13}$$

for simplicity, choose $\phi_i = 0$, so that the central axis of the $+z$ polarized magnet whose index is $s = 0$ corresponds to the Cartesian x-axis ($\phi = 0$). Since there are $N_m/4$ Halbach arrays in the disk, the electrical frequency becomes $N_m\omega/4$. Using equation (5) and Faraday's law, the open circuit voltage becomes

$$\begin{aligned} V_{oc}(t) &= -\frac{d\hat{\Phi}_{r-z}(t)}{dt} = -\frac{d}{dt}\left(\Phi_{\max,r-z}\sin\left(-\frac{N_m}{4}\omega t\right)\right) \\ &= \frac{N_m}{4}\omega\Phi_{\max,r-z}\cos\left(\frac{N_m}{4}\omega t\right) \end{aligned} \tag{14}$$

whose peak value at time $t = 0$ is

$$V_{oc,\max} = \frac{N_m}{4}\omega\Phi_{\max,r-z} \tag{15}$$

computing the maximum current from equation (10) and the complex impedance of the winding via Ohm's law gives

$$I_{\max} = \frac{V_{oc,\max}}{\sqrt{R_{tot}{}^2 + \left(\frac{N_m}{4}\omega L_{tot}\right)^2}} = \frac{\frac{N_m}{4}\omega\Phi_{\max,r-z}}{\sqrt{R_{tot}{}^2 + \left(\frac{N_m}{4}\omega L_{tot}\right)^2}} \tag{16}$$

with R_{tot} and L_{tot} representing the total resistance and inductance, respectively, of the stator winding circuit, including the stator self-resistance, R_s, self-inductance, L_s, plus any external passive components. Typically, an external coil with resistance R_c and inductance L_c is added in series with the stator winding. The purpose of the coil is to optimize the phase shift of the voltage and current, which maximizes axial force production (lift) while minimizing transverse plane force production (drag). For the arrangement under consideration, it is necessary that the phase angle between the voltage and current be as close to $\pi/2$ as practical so that the current is flowing radially outward ($+r$) when a $+\phi$ polarized magnet is passing over the stator so that lift force *(-z)* may be produced. Adding the coil resistance and inductance gives $R_{tot} = R_s + R_c$ and $L_{tot} = L_s + L_c$ which gives the amplitude of the winding current as

$$I_{\max} = \frac{\frac{N_m}{4}\omega\Phi_{\max,r-z}}{\sqrt{(R_s + R_c)^2 + \left(\frac{N_m}{4}\omega(L_s + L_c)\right)^2}} \tag{17}$$

The current may be decomposed into its imaginary (lift-producing) and real (drag-producing) components:

$$I_{Lift}(t) = \left[\frac{N_m}{4}\omega\Phi_{\max,r-z}\right]\frac{\frac{N_m}{4}\omega(L_s + L_c)}{(R_s + R_c)^2 + \left(\frac{N_m}{4}\omega(L_s + L_c)\right)^2}\sin\left(\frac{N_m}{4}\omega t\right) \tag{18}$$

$$I_{Drag}(t) = \left[\frac{N_m}{4} \omega \Phi_{\max, r-z} \right] \frac{R_s + R_c}{(R_s + R_c)^2 + \left(\frac{N_m}{4} \omega (L_s + L_c) \right)^2} \cos(\frac{N_m}{4} \omega t) \tag{19}$$

Note that the lift current is in phase with the inverse of the B_ϕ field component given in equation (7) and the drag current is in phase with the B_z component given in equation (8). In order to approximate the Lorentz force on the stator winding using *dF = Idl x B,* one first requires the spatial averages of the peak field components over the radial span of the top of the winding.

$$B_{\phi avg, top} = \frac{-1}{R_2 - R_1} \int_{R_1}^{R_2} B_\phi(r, \omega t = \pi/2, z = -g) dr \tag{20}$$

$$B_{z avg, top} = \frac{1}{R_2 - R_1} \int_{R_1}^{R_2} B_z(r, \omega t = 0, z = -g) dr \tag{21}$$

These expressions have straightforward numerical solutions. B_ϕ is a sinusoidal function with amplitude $B_{\phi avg, top}$ and B_z is a co sinusoidal function with amplitude $B_{z avg, top}$. The time average of the product of two in-phase sinusoids is one-half the product of their amplitudes, so the Lorentz force becomes

$$F_{Lift, avg} = \frac{1}{2} B_{\phi avg, top} N_t w I_{Lift} W (1 - e^{-\frac{N_m}{2W} H}) \tag{22}$$

$$F_{Drag, avg} = \frac{1}{2} B_{z avg, top} N_t w I_{Drag} W (1 - e^{-\frac{N_m}{2W} H}) \tag{23}$$

The exponential factor at the end of each expression accounts for the bottom leg of the stator winding, where the current flows in the opposite direction and force production opposes the contribution from the top leg of the winding. From the previous expressions, it should be noted that both the lift and drag forces increase with the square of the magnet strength (B_r^2), the square of the number of stator turns (N_t^2) and the square of the winding factor (w^2). Force production falls off with gap distance *g* by a factor of e^{-2g}. The stator winding circuit resistances and inductances determine both the saturation value of the lift force and the rotational speed at which saturation is achieved. The drag force outpaces the lift force at low rotational speeds but reaches a maximum value at a critical speed

$$\omega_c = \frac{4}{N_m} \frac{R_s + R_c}{L_s + L_c} \tag{24}$$

and then rolls off toward zero at high speeds. The expressions for lift and drag force are per stator pole, so the net forces must be summed over all poles.

Flux, EMF, Current and Force Calculations for an *r-ϕ* Stator

For the *r-ϕ* stator the analysis proceeds in a similar way. Consider a stator pole piece which is sector-shaped and wound horizontally, i.e., the plane of the center of the stator winding lies in the *r-ϕ* plane

centered at azimuthal location $\phi = 0$. The normal vector of this plane coincides with the z direction. The winding consists of N_t turns and the width of the winding in the radial direction is W. The winding spans an angle β in the azimuthal direction. W is again chosen to be approximately the magnet width. β is chosen to be exactly the angular span of two magnets or $\beta = 4\pi/Nm$ so that each radial leg of the winding will carry a current that is in phase with the B_ϕ component to produce lift. A gap, g, exists between the bottom surface of the magnets and the center of the top conductors of the winding. Figure 3 illustrates these concepts from a view located below the winding.

The stator flux for this configuration is

$$\Phi_{r-\phi}(\phi) = N_t w \int_S B_z(\vec{r}) \bullet dS = N_t w \int_{R_1}^{R_2} \int_{-\frac{2\pi}{N_m}}^{\frac{2\pi}{N_m}} B_\phi(r,\phi,z)\, r\, d\phi\, dr \tag{25}$$

The winding factor, $w = w_1 w_2$, for a layer of $N_t = N_{tz} N_{t\phi}$ turns is still given by equations (3) and (4). The approximation of the stator flux becomes

$$\hat{\Phi}_{r-\phi}(\phi) = \left[\Phi_{r-\phi}(\phi)\Big|_{\phi=0} \right] \cos\left(\frac{N_m}{4}\phi\right) = \Phi_{\max, r-\phi} \cos\left(\frac{N_m}{4}\phi\right) \tag{26}$$

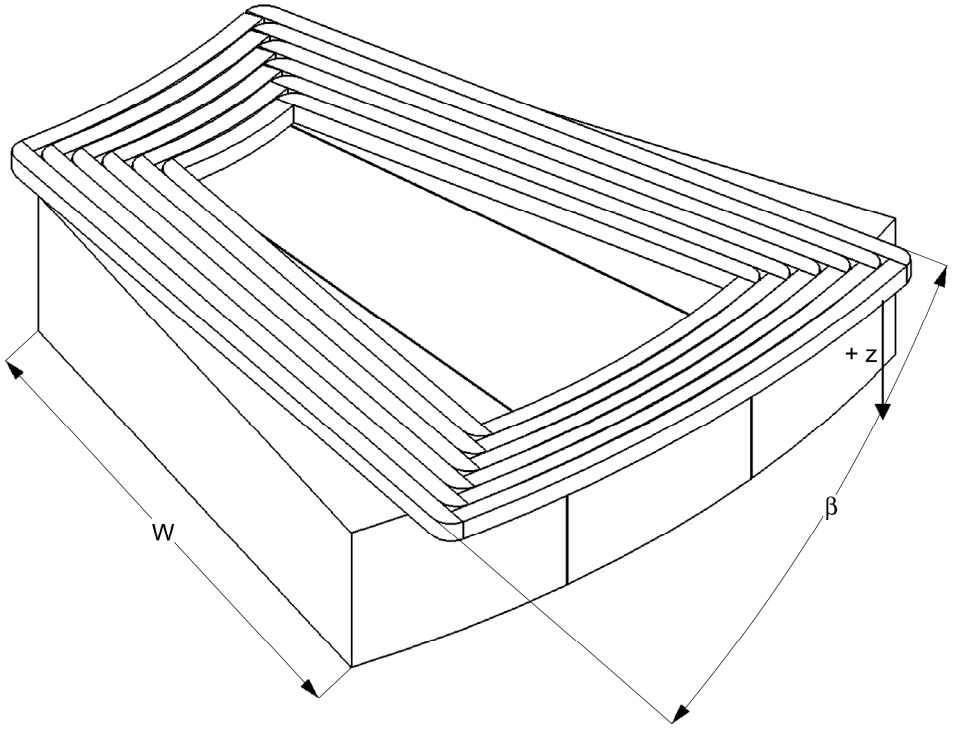

Figure 3.—The r-ϕ stator winding viewed from below the magnet array. The azimuthal span of the winding β matches the width of two magnets W refers to the winding width. A gap, g, (not shown) exists between the conductors of the winding and the magnet surface.

and the open circuit voltage becomes

$$V_{oc}(t) = -\frac{d\hat{\Phi}_{r-\phi}(t)}{dt} = -\frac{d}{dt}\left(\Phi_{\max,r-\phi}\cos\left(-\frac{N_m}{4}\omega t\right)\right) = -\frac{N_m}{4}\omega\Phi_{\max,r-\phi}\sin\left(\frac{N_m}{4}\omega t\right) \tag{27}$$

The voltage reaches a peak positive value at time $t = 6\pi/N_m\omega$ given by

$$V_{oc,\max} = \frac{N_t w N_m}{4}\omega\int_{-\frac{2\pi}{N_m}}^{\frac{2\pi}{N_m}}\int_{R_1}^{R_2} B_{zo}(r)\, e^{-\frac{N_m}{4r}z}\, r\, dr\, d\phi \tag{28}$$

The maximum current is found from the magnitude of the complex impedance as before

$$I_{\max} = \frac{V_{oc,\max}}{\sqrt{(R_s + R_c)^2 + \left(\frac{N_m}{4}\omega(L_s + L_c)\right)^2}} \tag{29}$$

where again $R_{tot} = R_s + R_c$ and $L_{tot} = L_s + L_c$ to account for any external inductance required to produce the desired phase shift between voltage and current. Interestingly, the r-ϕ stator has an inherent $-\pi/2$ phase shift arising from the geometry between the center of the winding and the current-carrying outer legs. However, this is negated by the inherent $\pi/2$ phase shift between the field producing the flux (B_z) and the field driving the lifting force (B_ϕ). Thus, it is still necessary that the phase angle between the voltage and current is as close to $\pi/2$ as practical so that the current is at its maximum value when $\pm\phi$ polarized magnets are passing over the two radial legs of the stator winding.

The current may again be decomposed into real (lift-producing) and imaginary (drag-producing) components:

$$I_{Drag}(t) = \frac{R_s + R_c}{(R_s + R_c)^2 + \left(\frac{N_m}{4}\omega(L_s + L_c)\right)^2} V_{oc,\max}\sin\left(\frac{N_m}{4}\omega t\right) \tag{30}$$

$$I_{Lift}(t) = \frac{\frac{N_m}{4}\omega(L_s + L_c)}{(R_s + R_c)^2 + \left(\frac{N_m}{4}\omega(L_s + L_c)\right)^2} V_{oc,\max}\cos\left(\frac{N_m}{4}\omega t\right) \tag{31}$$

Although the flux is now produced by the B_z component the lift force is still produced by the B_ϕ component. So the lift current is still in phase with the B_ϕ field component and the drag current is in phase with the B_z component. Unlike the r-z stator, the r-ϕ stator produces lift and drag forces in the same direction and of equal magnitude from both legs of the stator winding. This yields the following expressions for the average lift and drag forces.

$$F_{Lift,avg} = B_{\phi avg,top} N_t \, w I_{Lift} W \tag{32}$$

$$F_{Drag,avg} = B_{zavg,top} N_t \, w I_{Drag} W \tag{33}$$

As with the *r-z* stator case, both the lift and drag forces increase with the square of the magnet strength (B_r^2), the square of the number of stator turns (N_t^2) and the square of the winding factor (w^2). Force production falls off with gap distance *g* by a factor of e^{-2g}. The stator winding circuit resistances and inductances determine both the saturation value of the lift force and the rotational speed at which saturation is achieved. The drag force outpaces the lift force at low rotational speeds but reaches a maximum value at a critical speed

$$\omega_c = \frac{4}{N_m} \frac{R_s + R_c}{L_s + L_c} \tag{34}$$

and then rolls off toward zero at high speeds.

Comparative analysis of the two stator designs reveals that the force production per pole more than quadruples when the *r-*ϕ stator design is used. However, packaging constraints will permit only half as many *r-*ϕ stator poles as *r-z* poles. The net gain in force is therefore slightly more than doubled. However, this applies to both lift and drag forces, as well as to power dissipation. The gain in levitating force comes with no significant gain in lift/drag ratio and at the cost of increased real power dissipation and heating. The choice of stator design represents a tradeoff among these factors.

Test Objectives

The objective of testing the Axial Halbach Magnetic Bearing is to validate the derived theoretical analyses and associated finite element analyses. This validation provides confidence in using the derived and numerical analyses for developing and optimizing conceptual Axial Halbach Magnetic Bearing designs.

Testing of the Axial Halbach Magnetic Bearing was performed at NASA Glenn. Of particular interest is the performance of the bearing. Force, voltage, current, and temperature were monitored at various rotor operating speeds.

Test Hardware Description

The Axial Halbach Magnetic Bearing Test Model hardware is shown in figure 4 and a block diagram of the system is shown in figure 5. The Test Model components are identified in figure 6. This test hardware includes the support structure, force measurement scale and positioning system, and drive system components.

The support structure consists of precision modular structural components that are securely fastened to a heavy optics plate. The motor and the drive shaft bearing blocks are connected to right angle brackets that are connected to the optics plate via posts. This subsystem supports and aligns the drive system with respect to the force scale and positioning system that is placed on the optics plate. A safety shield is also incorporated into the support structure to protect personnel from the rotating components of the drive system and rotor.

The drive system consists of a variable speed computer-controlled servo motor that is connected to a one half inch diameter drive shaft through a flexible coupling to allow for misalignment. The drive shaft is supported by two roller bearings that are secured in the bearing blocks. The rotor assembly is pinned to the drive shaft and is driven by the motor to maintain precise operating speed.

Figure 4.—Axial Halbach magnetic bearing test model.

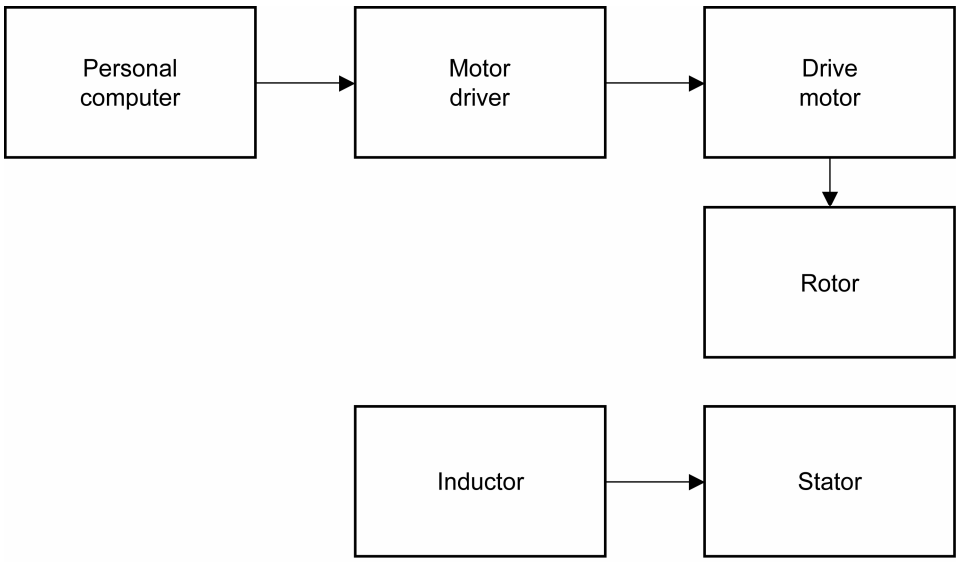

Figure 5.—Axial Halbach magnetic bearing test model block diagram.

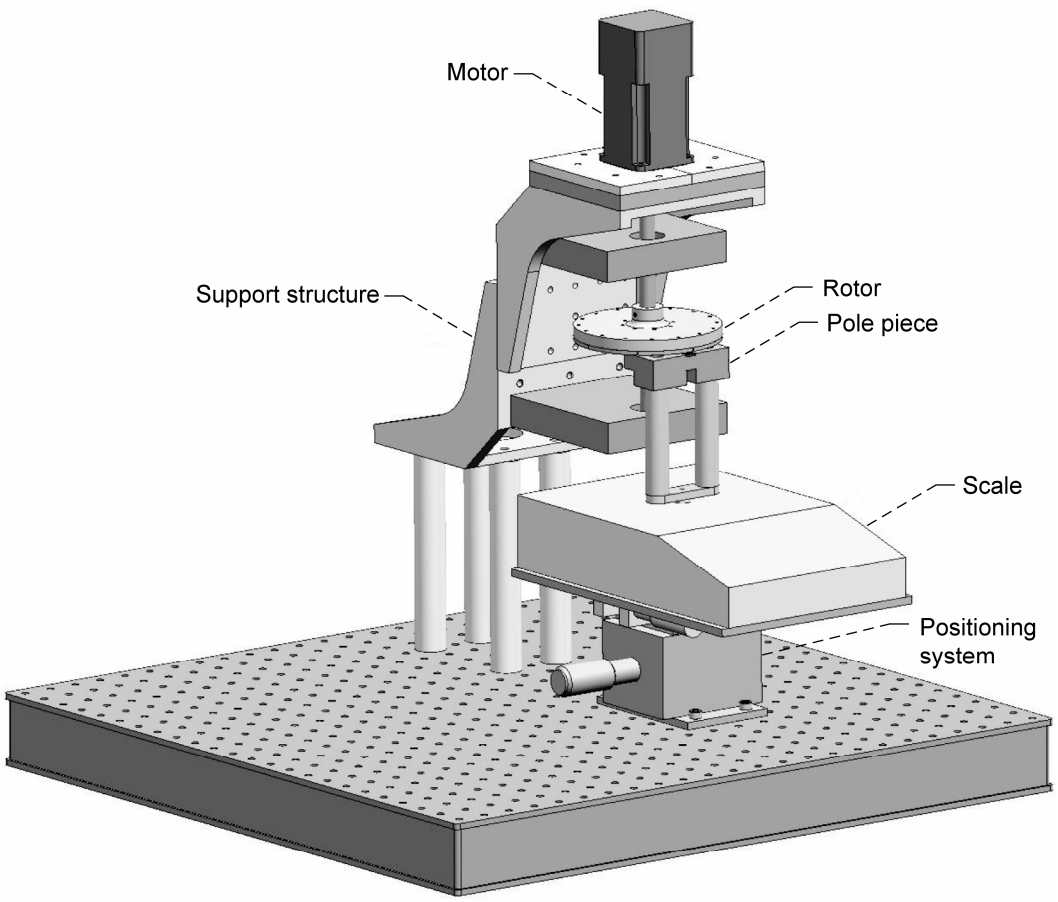

Figure 6.—Axial Halbach magnetic bearing test model components.

The rotor assembly, as shown in figures 7 and 8, consists of a 4.7 in. overall diameter aluminum hub that is bored out to contain 32 Neodymium Iron Boron (Nd) B55 magnets. The magnets are each 1 quarter in. thick by 1 in. long segments. The 32 segments comprise a ring with an outside diameter of 4 in. and inside diameter of 2 in. Each magnet segment occupies 11.25° of the assembled magnet ring. The magnets are covered by a total of eight 45° 300 series stainless steel segmented covers with each cover restraining four magnets. This segmented cover design was necessary due to the difficulty in handling and assembling the 32 magnets into a Halbach array since adjacent magnets repel each other. Four magnets were oriented in a Halbach array and held in position and the cover was fastened to the hub with non-magnetic stainless steel screws. The total mass of the assembled rotor is 660 g (1.46 lb).

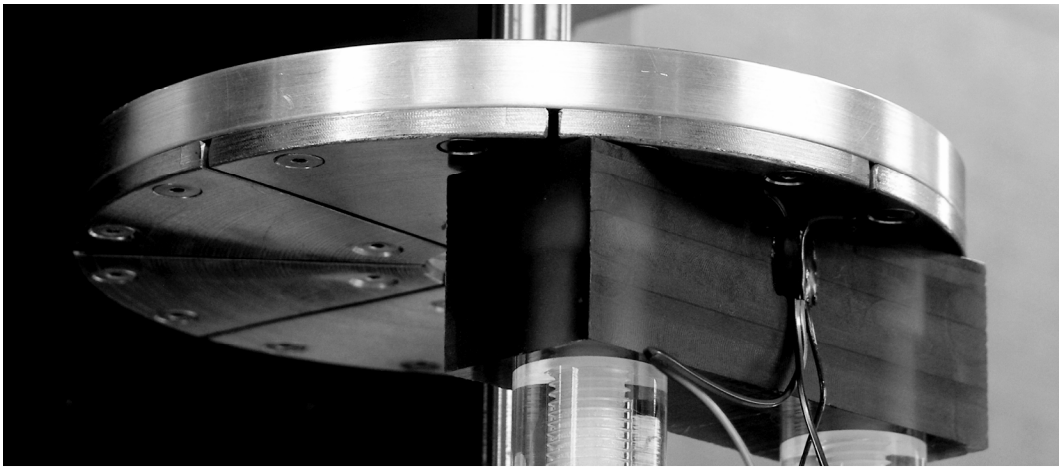

Figure 7.—Axial Halbach magnetic bearing test model rotor.

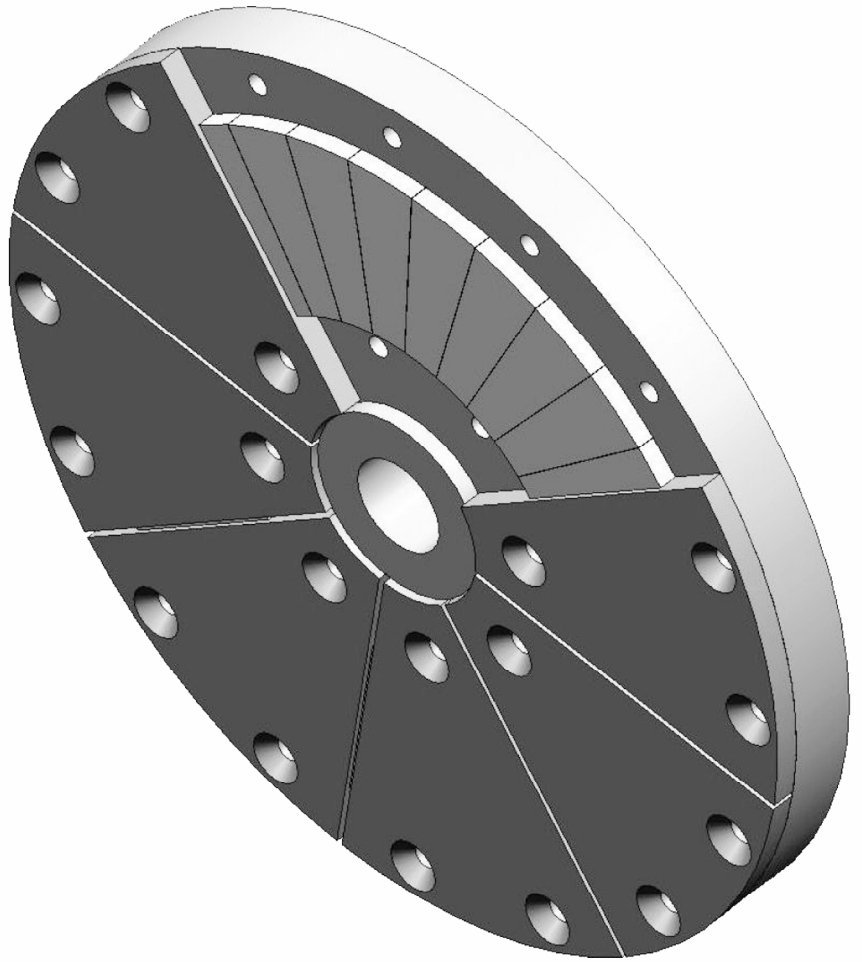

Figure 8.—Internal view of axial Halbach magnetic bearing rotor.

The rotation of the rotor causes the magnetic field to react with a coil of wire wound on the stator pole piece. Four different stator pole pieces were tested. Two *r-z* pole pieces were developed, one with one turn of wire, and the other with six turns of wire. Two *r-*ϕ pole pieces were also developed, one with one turn of wire and the other with six turns of wire. An *r-z* pole piece is shown in figure 9 and an *r-*ϕ pole piece is shown in figure 10. All of the pole pieces have 20 gauge square copper magnet wire. The wire is wound around a slot in the pole piece machined from Ultem polyetherimide with a maximum operating temperature of 340 °F. The magnet wire is cemented in place in the slot to ensure that accurate data is obtained.

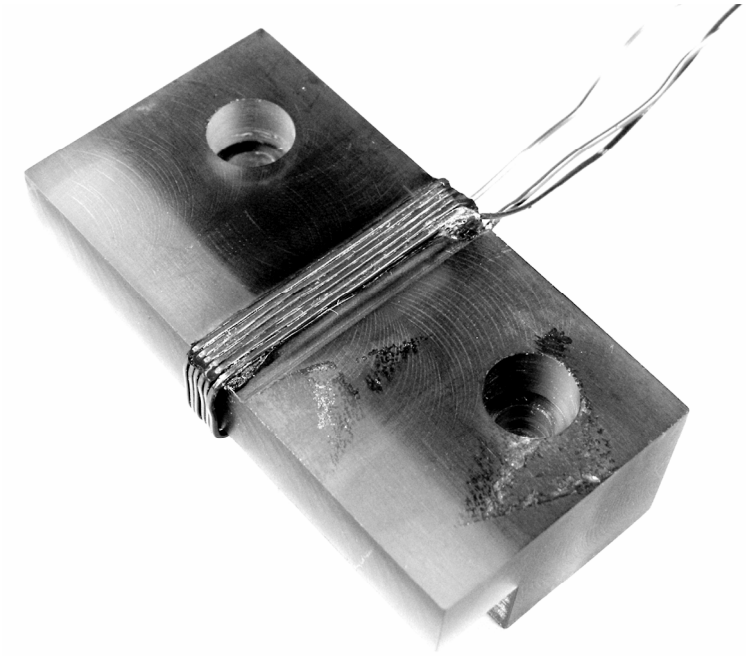

Figure 9.—Axial Halbach magnetic bearing test model r-z stator pole piece.

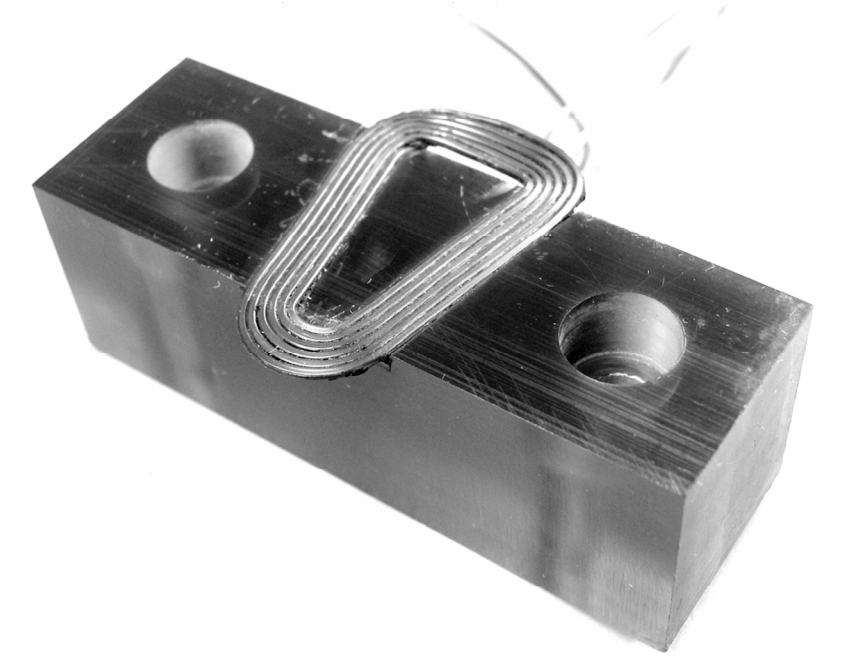

Figure 10.—Axial Halbach magnetic bearing r-ϕ stator pole piece.

The pole piece may be terminated by an inductor to introduce a phase shift to maximize the generated repulsive force. The inductor consists of 17 turns of 10 gauge square copper wire wound around a ferrite rod.

The orientation of the pole piece is highly critical. The pole piece is connected with nylon fasteners to a precision horizontal linear stage which is then connected to a precision vertical stage. These two stages allow for an accurate adjustment of the coil placement in close proximity to the surface of the rotor. The rotation of the Halbach array adjacent to the pole piece assembly generates a repulsive downward force on the force measurement scale.

Instrumentation

The Axial Halbach Magnetic Bearing Test Model was instrumented to measure bearing performance. Data from the drive motor, particularly rotor speed, were obtained from the motor drive system and sent directly to a personal computer (PC), where the data was stored. The other data were sent to the various test instruments and monitored. Test data included stator pole piece voltage, stator pole piece current, stator pole piece force, stator pole piece temperature, and ambient temperature.

A block diagram of the instrumentation system is shown in figure 11. Type K thermocouples were used for all temperature measurements. Hall Effect transducers were used for all current measurements.

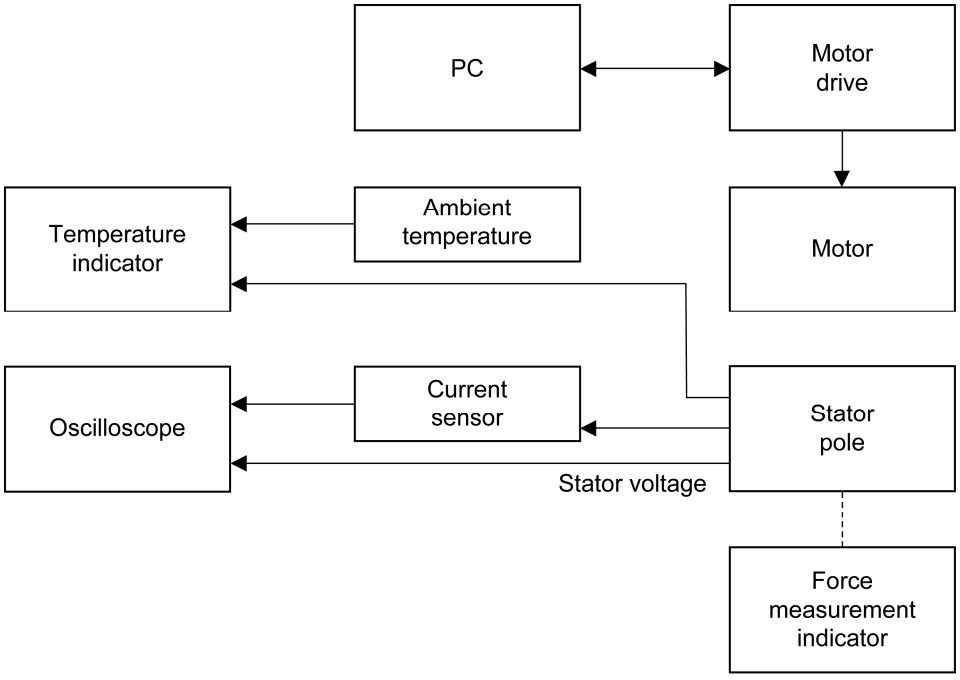

Figure 11.—Axial Halbach magnetic bearing instrumentation block diagram.

Test Procedures

The tests described in this report were conducted at the NASA Glenn Research Center in Cleveland, Ohio. The tests were conducted in accordance with the test matrix provided in table 1.

TABLE 1.—AXIAL HALBACH MAGNETIC BEARING TEST MATRIX

Parameter	Gap (in.)	Speed (rpm)	Termination
Six turn *r-z* stator pole	0.05, 0.08, 0.11	100, 200, 500, 1000, 2000, 3000	Open circuit, short circuit, inductor
Six turn *r-z* stator pole	0.05, 0.08, 0.11	100, 200, 500, 1000, 2000, 3000	Open circuit, short circuit, inductor
Single turn *r-*ϕ stator pole	0.05, 0.08, 0.11	100, 200, 500, 1000, 2000, 3000	Open circuit, short circuit, inductor
Six turn *r-*ϕ stator pole	0.05, 0.08, 0.11	100, 200, 500, 1000, 2000, 3000	Open circuit, short circuit, inductor

The test procedure used four different stator pole designs: single-turn *r-z* plane, 6-turns *r-z* plane, single turn *r-*ϕ plane and 6-turns *r-*ϕ plane. All four stators contain 20 AWG wire (d = 0.032 in. (0.8 mm)). The test consisted of precisely locating the stator beneath the magnet array such that the air gap was one of three selected values: 0.05 in. (1.3 mm), 0.08 in. (2.0 mm, and 0.11 in. (2.8 mm). Factoring in the thickness of the retaining cover plate and the finite radius of the conductor, the effective gap distances from the magnet surfaces to the center of the conductor were 0.096 in. (2.4 mm), 0.126 in. (3.2 mm, and 0.156 in. (4.0 mm), respectively. With the array rotating at fixed mechanical speeds of 100, 200, 500, 1000, 2000, and 3000 rpm, peak-to-peak open circuit voltage (V_{oc}) and short circuit current (Iss) were measured via an oscilloscope. With a series coil (17 turns, 10 AWG, L_c = 9.1 μH, R_c = 2.5 $m\Omega$) inserted into the stator winding circuit, current (I_c) and lift force (F_{lift}) production were measured with a precision scale.

The analytical model presented in this article predicted expected values for V_{oc}, I_{ss}, I_c, and F_{lift}. Predicted values were compared to the measured results. Additionally, the analytical model predicted the drag force (Fdrag) and power dissipation (Pd).

Finite element analysis (FEA) predictions at 500 and 2000 rpm at an air gap of 0.05 in. were also compared to the analytical and measured results for open-circuit voltage and short-circuit current. Maxwell 3D (Ansoft Corp.) was the software used to generate the FEA predictions.

Test Results

System Performance

Various tests were conducted to determine system performance, per table 1. Table 2 summarizes the results obtained at 500 rpm and table 3 summarizes the results obtained at 2000 rpm for the four different stator designs. A complete set of data for all rotational speeds is presented as a series of plots in appendix B.

TABLE 2.—AXIAL HALBACH MAGNETIC BEARING PERFORMANCE AT 500 rpm

At 500 rpm eff gap = 0.096 in. (2.5 mm)	1 Turn *r-z* stator			6 Turn *r-z* stator			1 Turn *r-*ϕ stator			6 Turn *r-*ϕ stator		
Quantity	Measured	Analytical predicted	FEA predicted	Measured	Analytical predicted	FEA predicted	Measured	Analytical predicted	FEA predicted	Measured	Analytical predicted	FEA predicted
V_{oc} (V)	0.046	0.047	0.046	0.231	0.249	0.260	0.095	0.100	0.12	0.562	0.588	0.7
I_{ss} (A)	6.2	6.0	5.9	11.8	11.1	11.7	8.8	9.9	11.0	24.7	26.2	32.0
I_{coil} (A)	4.6	4.4	N/A	9.8	10.0	N/A	7.2	7.6	N/A	27.0	30.2	N/A
F_{lift} (N) with coil	N/A	0.005	N/A	0.028	0.028	N/A	0.013	0.014	N/A	0.172	0.18	N/A
F_{drag} (N) with coil	N/A	0.013	N/A	N/A	0.168	N/A	N/A	0.045	N/A	N/A	0.91	N/A
P_d (W) with coil	N/A	0.042	N/A	N/A	0.582	N/A	N/A	0.167	N/A	N/A	3.59	N/A

TABLE 3.—AXIAL HALBACH MAGNETIC BEARING PERFORMANCE AT 2000 rpm

At 2000 rpm eff gap = 0.096 in. (2.5 mm)	1 Turn *r-z* stator			6 Turn *r-z* stator			1 Turn *r-*ϕ stator			6 Turn *r-*ϕ stator		
Quantity	Measured	Analytical predicted	FEA predicted	Measured	Analytical predicted	FEA predicted	Measured	Analytical predicted	FEA predicted	Measured	Analytical predicted	FEA predicted
V_{oc} (V)	0.18	0.19	0.175	0.94	1.00	0.96	0.36	0.40	0.49	2.22	2.35	3.00
I_{ss} (A)	23.4	24.8	23.3	42.20	43.86	42.0	34.00	39.98	49.00	105.00	118.74	144.0
I_{coil} (A)	10.00	10.22	N/A	32.50	32.48	N/A	19.00	20.17	N/A	77.50	80.79	N/A
F_{lift} (N) with coil	0.03	0.03	N/A	0.27	0.30	N/A	0.09	0.09	N/A	1.24	1.74	N/A
F_{drag} (N) with coil	N/A	0.02	N/A	N/A	0.46	N/A	N/A	0.08	N/A	N/A	2.17	N/A
P_d (W) with coil	N/A	0.00	N/A	N/A	4.43	N/A	N/A	0.51	N/A	N/A	20.26	N/A

Discussion

The objective was to verify the analytical model of the axial Halbach array presented in this article by comparing both measured results and FEA-predicted results. The analytical model effectively predicts induced EMF, current and lifting force in the stator pole at lower speeds. At higher speeds, the combined effects of temperature rise and skin effect (both of which tend to increase the effective resistance of the stator winding) attenuate the current and lifting force. Saturation of the ferrite core in the external series inductor limits the amount of phase shift that can be achieved above around 50 amps of total current. This also contributes to losses in force production.

The *r-*ϕ stator produces about 5 times the net lifting force compared to the *r-z* stator. This is due to three effects. First, the B_z field is slightly stronger (~2 percent) than the B_ϕ field. Second, the proximity of the entire flux plane to the magnets in the *r-*ϕ case produces more efficient flux linkage in the stator winding. Finally, both legs of the stator winding contribute to force production harmoniously in the *r-*ϕ case, whereas the bottom leg of the *r-z* winding produces forces in opposition to the forces produced by the top leg. It should be noted, however, that commensurate increases in drag force and power dissipation will also occur with the *r-*ϕ design. Additionally, packaging constraints tend to limit the number of poles that may be wound in the *r-*ϕ configuration to about one-half of the number of equivalent *r-z* poles. The physical and electrical constraints of the application of the axial Halbach magnetic bearing will usually determine the appropriate choice of stator orientation.

These results were obtained using a small-scale test model. The factors limiting performance of this model actually improve dramatically when the physical scale is increased by an order of magnitude. First, the available space for packaging stator windings increases, permitting the use of lower gauge wire (less R), a higher number of turns (more L), or both. Increasing the radial span (W) of the stator winding gives a net gain in force production since F_{lift} increases with W_2, while the winding resistance only increases linearly with W. This is due to the fact that W figures linearly into both the stator current calculation and the Lorentz force calculation. For large machines on the order of 1 m diameter, the stator inductance to resistance ratio may be made favorable enough to make the use of an external series inductor unnecessary, even at speeds of less than 1000 rpm. This favorable balance results in less resistive heating and the larger size gives more thermal mass, as well as more surface area from which to radiate heat.

Concluding Remarks

The NASA Glenn Research Center has successfully designed, developed, analyzed, and tested a revolutionary Axial Halbach Magnetic Bearing. The goals of the project include improving aircraft efficiency, reliability, and safety. The objective of this work is to develop a viable non-contact magnetic thrust bearing utilizing Halbach arrays for all-electric flight, and many other applications. This concept will help to reduce harmful emissions, reduce the Nation's dependence on fossil fuels and mitigate many

of the concerns and limitations encountered in conventional axial bearings such as bearing wear, leaks, seals, and friction loss. The Axial Halbach Magnetic Bearing is inherently stable and requires no active feedback control system or superconductivity as required in many magnetic bearing designs. The Axial Halbach Magnetic Bearing is useful for very high speed applications where conventional bearings cannot be used including turbines, instrumentation, and medical applications.

Theoretical derivations have been developed successfully to predict the levitation forces generated by a circular Halbach array and coil assembly. Finite element analyses successfully validated the theoretical derivations. Empirical test results obtained from experimental hardware successfully validated the basic principles described, and the theoretical work that was performed. Of particular value, are the analytical tools and capability that were developed successfully under this project. Performance predictions can be made confidently for machines of various scale.

The test results were obtained using a small scale test model. The factors limiting performance of this model improve significantly when the physical scale is increased. For large machines on the order of 1 m diameter, the stator inductance to resistance ratio may be made favorable enough to make the use of an external series inductor unnecessary, even at speeds of less than 1000 rpm. This favorable balance results in less resistive heating and the larger size gives more thermal mass, as well as more surface area from which to radiate heat.

The report concludes that the implementation of Axial Halbach Magnetic Bearings can provide significant improvements in rotational system performance and reliability. In addition to aircraft engines, this technology has potential application in ultra-efficient motors, computer memory systems, instrumentation systems, medical systems, manufacturing equipment, and space power systems, such as generators and flywheels.

References

1. Thompson, William K., “Three-dimensional field solutions for multi-pole cylindrical Halbach arrays in an axial orientation,” NASA/TM—2006-214359.
2. Post, R.F. and Ryutov, D.D., “The Inductrack, a simpler approach to magnetic levitation,” *IEEE Trans. Appl. Supercond.*, vol. 10(1), March 2000, pp. 901–4.

Appendix A
Equipment Under Test Summary Data Sheet

1.0 Axial Halbach Magnetic Bearing Test Model

1.1 Drive Motor

1.1.1	Type	Brushless DC Servo
1.1.2	DC Voltage Range	20 to 48 V
1.1.3	Operating Temperature	0 to 70 °C (32 to 158 °F)
1.1.4	Storage Temperature	–20 to 85 °C (–4 to 185 °F)
1.1.5	Humidity	0 to 80 percent
1.1.6	Peak Torque	0.63 N-m (89 oz-in.)
1.1.7	Continuous Torque	0.24 N-m (33 oz-in.)
1.1.8	No Load Speed	7400 rpm
1.1.9	Nominal Power	0.10 kW (0.14 HP)
1.1.10	Servo Update	4069 Hz
1.1.11	Rotor Inertia	1.34×10^{-5} kg-m^2 (0.0019 oz-in.^{2})
1.1.12	Width	57.2 mm (2.25 in.)
1.1.13	Length	115 mm (4.5 in.)
1.1.14	Weight	0.95 kg (2.1 lb)

1.2 Force Measurement System

1.1.2	Type	Variable Capacitance
1.1.3	Capacity	410 g
1.1.4	Readability	0.001 g
1.1.5	Linearity	±0.02 g

2.0 Rotor

2.1	Diameter	11.94 cm (4.7 in.)
2.2	Weight	660 g (1.46 lb)
2.3	Magnet Type	Neodymium Iron Boron B55
2.4	Magnet Orientation	Halbach Array
2.5	Magnet Shape	Sectors

3.0 Single Turn *r-z* Stator Pole Piece

3.1	Wire	20 Square Copper
3.2	Inductance	0.08 μH
3.3	Resistance	7.55 $m\Omega$

4.0 Six Turn *r-z* Stator Pole Piece

4.1	Wire	20 Square Copper
4.2	Inductance	1.90 μH
4.3	Resistance	22.50 $m\Omega$

5.0. Single Turn *r-*ϕ Stator Pole Piece

5.1	Wire	20 Square Copper
5.2	Inductance	0.085 μH
5.3	Resistance	10.00 $m\Omega$

6.0 Six Turn *r-*ϕ Stator Pole Piece

5.1	Wire	20 Square Copper
5.2	Inductance	2.34 μH
5.3	Resistance	19.42 $m\Omega$

7.0 Inductor

7.1	Configuration	Helix
7.2	Wire	10 Square Copper
7.3	Number of Turns	17
7.4	Core	Ferrite Rod
7.5	Inductance	9.1 μH
7.6	Resistance	2.5 $m\Omega$

Appendix B
System Performance Test Results

A complete set of plots of the test results are included here. Table 1 identifies the tests that were conducted.

REPORT DOCUMENTATION PAGE

Form Approved
OMB No. 0704-0188

1. AGENCY USE ONLY (*Leave blank*)	2. REPORT DATE	3. REPORT TYPE AND DATES COVERED
	July 2006	Technical Memorandum

4. TITLE AND SUBTITLE

Development and Testing of an Axial Halbach Magnetic Bearing

5. FUNDING NUMBERS

WBS 561581.02.08.03.06.04

6. AUTHOR(S)

Dennis J. Eichenberg, Christopher A. Gallo, and William K. Thompson

7. PERFORMING ORGANIZATION NAME(S) AND ADDRESS(ES)

National Aeronautics and Space Administration
John H. Glenn Research Center at Lewis Field
Cleveland, Ohio 44135–3191

8. PERFORMING ORGANIZATION REPORT NUMBER

E–15632

9. SPONSORING/MONITORING AGENCY NAME(S) AND ADDRESS(ES)

National Aeronautics and Space Administration
Washington, DC 20546–0001

10. SPONSORING/MONITORING AGENCY REPORT NUMBER

NASA TM—2006-214357

11. SUPPLEMENTARY NOTES

Responsible person, Dennis J. Eichenberg, organization code DEE, 216–433–8360.

12a. DISTRIBUTION/AVAILABILITY STATEMENT

Unclassified - Unlimited
Subject Category: 07

Available electronically at http://gltrs.grc.nasa.gov

This publication is available from the NASA Center for AeroSpace Information, 301–621–0390.

12b. DISTRIBUTION CODE

13. ABSTRACT ***(Maximum 200 words)***

The NASA Glenn Research Center has developed and tested a revolutionary Axial Halbach Magnetic Bearing. The objective of this work is to develop a viable non-contact magnetic thrust bearing utilizing Halbach arrays for all-electric flight, and many other applications. This concept will help to reduce harmful emissions, reduce the Nation's dependence on fossil fuels and mitigate many of the concerns and limitations encountered in conventional axial bearings such as bearing wear, leaks, seals and friction loss. The Axial Halbach Magnetic Bearing is inherently stable and requires no active feedback control system or superconductivity as required in many magnetic bearing designs. The Axial Halbach Magnetic Bearing is useful for very high speed applications including turbines, instrumentation, medical systems, computer memory systems, and space power systems such as flywheels. Magnetic fields suspend and support a rotor assembly within a stator. Advanced technologies developed for particle accelerators, and currently under development for maglev trains and rocket launchers, served as the basis for this application. Experimental hardware was successfully designed and developed to validate the basic principles and analyses. The report concludes that the implementation of Axial Halbach Magnetic Bearings can provide significant improvements in rotational system performance and reliability.

14. SUBJECT TERMS

Magnetic bearings

15. NUMBER OF PAGES

28

16. PRICE CODE

17. SECURITY CLASSIFICATION OF REPORT	18. SECURITY CLASSIFICATION OF THIS PAGE	19. SECURITY CLASSIFICATION OF ABSTRACT	20. LIMITATION OF ABSTRACT
Unclassified	Unclassified	Unclassified	